Monthly Notices of the ROYAL ASTRONOMICAL SOCIETY

MNRAS **525,** 183–189 (2023) https://doi.org/10.1093/mnras/stad2303
Advance Access publication 2023 July 28

Ton S 415: a close binary containing an intermediate helium subdwarf discovered with SALT and *TESS*

E. J. Snowdon [1]★ C. S. Jeffery [1] S. Schlagenhauf,[1] M. Dorsch[2,3] and I. M. Monageng [4,5]

[1]*Armagh Observatory and Planetarium, College Hill, Armagh BT61 9DB, UK*
[2]*Institut für Physik und Astronomie, Universität Potsdam, Haus 28, Karl-Liebknecht-Str. 24/25, D-14476 Potsdam-Golm, Germany*
[3]*Dr Karl Remeis-Observatory & ECAP, Friedrich-Alexander University Erlangen-Nürnberg, Sternwartstr. 7, D-96049 Bamberg, Germany*
[4]*South African Astronomical Observatory, P.O. Box 9, Observatory Rd., Observatory 7935, Cape Town, South Africa*
[5]*Department of Astronomy, University of Cape Town, Private Bag X3, Rondebosch 7701, South Africa*

Accepted 2023 July 25. Received 2023 June 23; in original form 2023 April 3

ABSTRACT

Hot subdwarfs are early-type low-mass stars lying between the main sequence and the white dwarf sequence. The majority have helium-burning cores and helium-poor surfaces. A minority have helium-rich surfaces. A few, including Ton S 415, have surfaces with between 10 per cent and 90 per cent helium (by number). Their properties are diverse and their origins mostly unknown. Ton S 415 was identified as a suspected binary in a Southern African Large Telescope (SALT) survey of hot subdwarfs from its large radial velocity. Using SALT spectroscopy and *Transiting Exoplanet Survey Satellite* light curves, we confirm that Ton S 415 is a close binary with an orbital period $p = 84.6460 \pm 0.0004$ min and velocity semi-amplitude $K = 175.5 \pm 1.0\,\mathrm{km\,s^{-1}}$. Analysis of the SALT spectrum and broad-band spectral energy distribution shows the visible star to have an effective temperature $T_{\rm eff} = 43\,300 \pm 1000$ K, surface gravity $\log g/\mathrm{cm\,s^{-2}} = 5.89 \pm 0.10$, surface helium-to-hydrogen ratio $\log y = -0.62 \pm 0.10$, radius $R = 0.1074 \pm 0.0025\,R_\odot$, and mass $M = 0.33 \pm 0.09\,\mathrm{M}_\odot$. By modelling the light curve, we estimate the binary mass ratio to be $q = 0.7 \pm 0.3$ and infer an unseen white dwarf companion with a mass of $M_{\rm WD} = 0.47 \pm 0.24\,\mathrm{M}_\odot$. The results are consistent with a post-common-envelope binary that lost its hydrogen envelope before reaching the peak of the red giant branch, becoming a hot subdwarf with a non-canonical mass. We predict that the system will evolve into a double white dwarf binary before eventually either forming a stably accreting AM CVn system, or merging to form an R CrB star.

Key words: (*stars*:) binaries: close – stars: chemically peculiar – stars: horizontal branch – *(stars:)* subdwarfs.

1 INTRODUCTION

The hot subdwarf stars are a diverse population of subluminous, low-mass, stars located around the blue end of the horizontal branch and between the main sequence and the white dwarf sequence. They can be broadly categorized into three groups. Most have helium-poor atmospheres, in which atomic diffusion processes have caused the helium to settle below a hydrogen-rich surface. The atmospheric helium abundance is very small, typically ≤ 1 per cent by number (Heber et al. 1984). About 10 per cent of the subdwarf population have helium-rich atmospheres (Green, Schmidt & Liebert 1986). Of these, ~ 95 per cent have extremely high helium surface abundances (≥ 80 per cent helium by number). The third group shows surface helium abundances between 5 per cent and 80 per cent (Naslim et al. 2010), or intermediate between the helium-poor and extremely helium-rich groups.

How hot subdwarfs form and evolve remains an important question. Han et al. (2002, 2003) proposed three main formation channels; common-envelope (CE) evolution, stable Roche-lobe overflow (RLOF), and the merger of two He white dwarfs. CE and RLOF produce subdwarfs with H-rich envelopes in close ($\sim$0.1−10 d) and wide ($\sim$10−1000 d) binaries, respectively. In the CE channels, the companion star is typically either a white dwarf or a low-mass main sequence star. Both CE and RLOF channels are expected to yield subdwarfs with masses close to the red-giant helium-ignition mass of $0.47\,\mathrm{M}_\odot$. More massive progenitors of $\gtrsim 2.3\,\mathrm{M}_\odot$ can undergo early, non-degenerate helium ignition, creating subdwarfs with sub-canonical masses. White dwarf mergers are more likely to produce single subdwarfs with extremely helium-rich surfaces and a wider range of potential masses (Zhang & Jeffery 2011)

The rarer intermediate helium (iHe) subdwarfs are harder to explain. Naslim et al. (2012) proposed that the iHe binary CPD−20°1123, a post-common-envelope system with an orbital period of 2.3 d, is the precursor to a normal B subdwarf (sdB), in which the helium dredged up on the giant branch has not yet settled below hydrogen in the envelope. If so, the binary fraction for iHe subdwarfs and normal sdBs should be similar. However, while around 60 per cent of sdB stars are known to be short-period post common-envelope binaries (Maxted et al. 2001), the fraction of short-period binary iHe subdwarfs appears to be much smaller.

A few iHe sdOB stars have been found in highly compact binaries. Kupfer et al. (2017) identified OW J074106.0-294811.0 as an sdOB star with $\log y \equiv \log n_{\rm He}/n_{\rm H} = -0.14 \pm 0.07$, orbiting a white dwarf companion with a period of 44.66 min. They concluded that the sdOB component is a post-CE He-WD with a mass of $0.32\,\mathrm{M}_\odot$, and the system will eventually either merge into an R CrB star, or become a stably accreting AM CVn system. Kupfer et al. (2020)

★ E-mail: Edward.snowdon@armagh.ac.uk

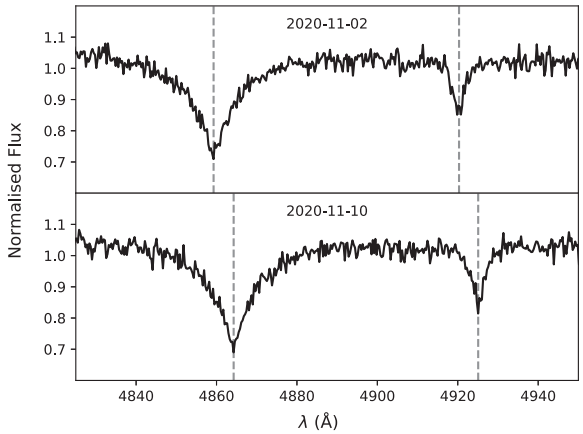

Figure 1. Sections of SALT RSS spectra for Ton S 415 taken on 2020 November 02 (top) and 2020 November 10 (bottom), showing Doppler shifts in the H_β (left) and He I 4921 Å (right) lines. The shift corresponds to a radial velocity difference of $\Delta v_{\rm rad} \simeq 292\,{\rm km\,s^{-1}}$ between observations.

identified ZTF J2130+4420 as a $0.34\,M_\odot$ sdOB star accreting onto a $0.55\,M_\odot$ CO-WD companion, with an orbital period of 39.34 min. They determined that the sdOB component is undergoing hydrogen shell burning and will evolve to a white dwarf and will eventually merge with its companion, resulting in either a supernova or an R CrB star.

Ton S 415 first appears in the Tontanzintla catalogue of 419 blue stars near the South Galactic Pole (Chavira 1958), where it is recorded as 'very violet'. Its Strömgren colours were measured by Wegner (1979, 1980), who found it 'unlikely to be degenerate'. Its spectrum was first obtained in the Edinburgh-Cape Blue Object Survey as EC 05160−3050. It was classified 'sdO' by Stobie, Kilkenny & O'Donoghue (1995), and later as 'He-sdO' (O'Donoghue et al. 2013a).

Taking a list of helium-rich subdwarfs from the EC survey as its original input catalogue, Ton S 415 was observed during the Southern African Large Telescope (SALT) survey of He-rich hot subdwarfs (Jeffery, Miszalski & Snowdon 2021). Its spectral type was measured as sdO8VII:He30 Drilling et al. (2013), making it an intermediate He-sdO star. It was found to have effective temperature $T_{\rm eff}/({\rm kK}) = 43.92 \pm 0.10$, surface gravity $\log g/({\rm cm\,s^{-2}}) = 5.96 \pm 0.04$, and surface helium abundance $\log y = -0.45 \pm 0.01$. Ton S 415 was identified as a possible binary from a high radial velocity measurement of $233\,{\rm km\,s^{-1}}$.

Inspection of two separate observations showed a large Doppler shift (Fig. 1), confirming the star as a binary and prompting follow-up observations to determine its orbit. This paper presents a spectroscopic and photometric analysis confirming Ton S 415 to be a binary iHe sdO star with an unseen white dwarf companion. We combine a radial velocity study of SALT optical spectra with light curve modelling to estimate the orbital parameters of the system and their uncertainties. We compare Ton S 415 to other iHe sdO binaries, and discuss the implications these objects have for the evolution of iHe subdwarfs.

2 OBSERVATIONS

2.1 *TESS* light curves and periodogram

Ton S 415 was observed by the *Transiting Exoplanet Survey Satellite* (*TESS*) in sectors 06 (2018) and 32 (2020) at 120 s cadence with durations of 21.77 and 25.83 d, respectively. The signal-to-noise

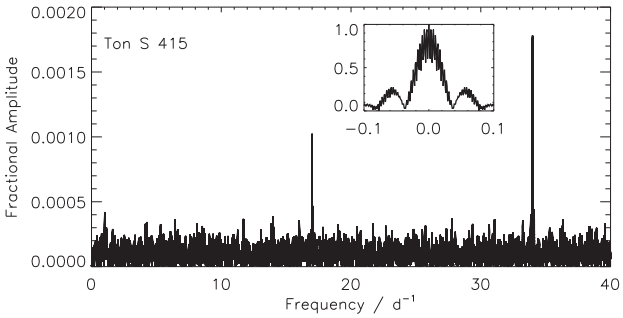

Figure 2. Amplitude–frequency spectrum of detrended *TESS* observations of Ton S 415 with window function in inset panel.

ratios were 93.99 for sector 06 and 87.64 for sector 32, based on the flux errors. Light curves were obtained from the Mikulski Archive for Space Telescopes (MAST) portal.[1] Light-curve manipulation and analysis was done using the LIGHTKURVE PYTHON package (Lightkurve Collaboration 2018). No flux contamination from other stars was assumed, since there are no bright sources within 10 arcsec of Ton S 415. The instrumental low-frequency trend was corrected using a Savitzky–Golay filter with a window length of 213 (approx. five times the period) and a polynomial order of two (Savitzky & Golay 1964). Data points that differed from the mean by more than 3σ were removed as outliers. A Lomb–Scargle periodogram constructed using these light curves showed broad peaks at frequencies of ∼17 and ∼34 cycles $\rm d^{-1}$. Aliases due to inter-sector gaps produce a fine-structure frequency spacing of $0.00144\,{\rm d^{-1}}$ (Fig. 2). The window function has multiple closely spaced aliases corresponding to the inverse of the time interval between the *TESS* sectors. The 2:1 frequency ratio of the peaks indicates ellipsoidal modulation caused by deformation of the iHe star (Morris 1985), with the lower frequency peak corresponding to an orbital period of ∼ 85 min.

Neither the light curve nor spectrum of Ton S 415 contain direct evidence for the nature of its companion star. Ellipsoidal modulation suggests an unseen compact companion. While neutron star companions to hot subdwarfs have been predicted by population synthesis models (Wu et al. 2018), based on its mass, it is most likely that the second component of Ton S 415 is a white dwarf.

2.2 SALT RSS spectra

Observations of Ton S 415 for the SALT survey were obtained in November 2020 using the Robert Stobie Spectrograph (RSS) with the PG2300 grating at grating angles of 30.5° and 32° yielding a spectral resolution $R \simeq 3000-3800$ in the wavelength range $\lambda\lambda = 3850-5150$ Å at a slit width of 1.0 Å. Two object frames and one CuAr arc frame were obtained at each grating position. 60 s exposure times were used for all frames. Spectra were extracted from each object frame and combined. The combined spectra were used for classification of the star, coarse analysis, and identification of radial velocity shifts.

Once an orbital period had been determined from the *TESS* periodogram, additional RSS observations were made in 2022 August–September to determine the projected orbital velocity. To maximize phase coverage, data were taken in sequences of up to 24 object frames, with arc frames taken before, after 12 frames, and at the end of each run. Since continuous spectra were not needed, only the 30.5° grating angle was used. Longer sequences were not practicable

[1] https://mast.stsci.edu/

Table 1. Record of SALT RSS observations for Ton S 415; exposure time was 60 s in all cases.

Date	UT start	UT end	Exposures
2020-11-02	22:25:21	22:31:44	4
2020-11-10	21:31:32	21:41:58	4
2022-08-16	03:16:40	03:53:33	21
2022-08-23	02:37:18	03:11:01	24
2022-08-29	02:14:36	02:30:05	12
2022-09-08	01:48:19	02:22:40	24
2022-09-11	01:19:49	01:53:42	23

because of the limited viewing window allowed by the fixed-altitude design of SALT. A summary of all RSS observations of Ton S 415 is given in Table 1.

Reduction of the 2020 RSS data was described by Jeffery et al. (2021). The 2022 RSS data were reduced using the Titus Saures Rex pipeline[2] (Titus, priv. comm.). Cosmic ray removal was performed using the LACOSMIC package (van Dokkum 2001). The extracted 1D, sky-subtracted spectra were wavelength-calibrated by interpolating a custom arc frame from the lamp frames taken before and after the observing block, weighted based on the time gap between the image and arc exposures. This was done to compensate for potential changes in the wavelength calibration during the interval between arc frames due to flexure or thermal drift in the spectrograph. After calibration, barycentric corrections were applied to the wavelengths of the spectra. Normalization was done by fitting low-order polynomials to the continuum.

3 FUNDAMENTAL PARAMETERS

Initial estimates for the parameters of Ton S 415 were based on metal-free non-LTE model atmospheres (Jeffery et al. 2021). A substantial improvement can be obtained using the fully line-blanketed non-LTE model grid 'sdOstar' (Dorsch et al. 2021), from which we obtain $T_{\rm eff} = 43\,330$ K, $\log g/{\rm cm\,s^{-2}} = 5.89$, $\log y = -0.62$ and $v \sin i < 15\,{\rm km\,s^{-1}}$ (Fig. 3). Higher resolution data will be necessary to measure surface metal abundances confidently; from the weakness of C, N, and Si lines, they appear to be sub-solar.

Fundamental stellar parameters can be obtained by fitting the spectral energy distribution (SED) defined by multi-wavelength photometry to the same 'sdOstar' model grid (Fig. 4). The SED fitting method is described in more detail by Heber, Irrgang & Schaffenroth (2018). We consider interstellar extinction using the reddening law of Fitzpatrick et al. (2019), parametrized by the colour excess $E(44-55)$ and the ratio of total-to-selective extinction $R(55)$, which was fixed to the Milky Way mean value of 3.02. Comparing solutions with $T_{\rm eff}$ as a free SED fit parameter and fixed to the value obtained from the RSS spectrum leads to a marginal (3 per cent) difference in the stars' angular diameter, so we adopt the fixed solution. The angular diameter Θ obtained from the SED fit is then combined with the parallax measurement ϖ from *Gaia* EDR3 (El-Badry, Rix & Heintz 2021; Lindegren et al. 2021) and the spectroscopic $T_{\rm eff}$ and $\log g$ to derive the radius, luminosity, and mass. The results are summarized in Table 2.

[2]https://github.com/NaomiTitus

4 RADIAL VELOCITY ANALYSIS

The RSS spectra were used to construct a radial velocity curve for Ton S 415 by measuring the wavelength shift between observations by cross-correlation. Since the 2022 observations were taken at only one grating angle, there were two gaps in the spectra caused by the gaps between the three CCDs in the RSS camera. Each spectrum was therefore divided into three sections (4050–4400, 4450–4750, and 4800–5100 Å) which were analysed separately. The spectra were rebinned to a consistent, evenly spaced logarithmic wavelength axis and then cross-correlated with the spectrum taken at $t = 0$ (the time of the first observation). Parabolae were fitted to the peaks of the cross-correlation functions to determine rough radial velocity shifts $\Delta v_{\rm rad} = c\Delta \ln \lambda$ and associated errors. The spectrum sections in each wavelength range were then co-added to create high signal-to-noise ratio template spectra. Cross-correlation was then repeated using these templates to measure $\Delta v_{\rm rad}$ precisely.

To determine the non-orbital component of the radial velocity, the templates were cross-correlated with a model spectrum synthesized with $v_{\rm rad} = 0\,{\rm km\,s^{-1}}$. $\Delta v_{\rm rad}$ relative to the template was found to be 53.86, 30.2, and 21.11 $\rm km\,s^{-1}$ for the short-, middle-, and long-wavelength sections, respectively. The discrepancy in radial velocity between sections is caused by imperfections in the wavelength calibration. These values were subtracted from the measured $\Delta v_{\rm rad}$ for each spectrum segment. Orbital periods were selected from the sub-peaks of the $17\,{\rm d^{-1}}$ peak in the periodogram of the *TESS* light curves, aiming to minimize the phase shift between $\Delta v_{\rm rad}$ measurements from different sectors. This gave a more precise period result of 84.640 ± 0.0004 min ($0.05884656 \pm 0.00000025$ d), where the error derives from half the frequency spacing in the periodogram. By phasing to this period, we obtain a sinusoidal velocity curve of the form:

$$v_{\rm rad} = \gamma + K \sin\left(\frac{2\pi}{p}(t - T_0)\right), \quad (1)$$

where K is the radial velocity semi-amplitude, p is the orbital period, γ is the mean system velocity, and $T_0 = (\phi_0 p)/2\pi$ is the epoch of conjunction. Curve fitting was performed using RVLIN (Wright & Howard 2009), which fits an arbitrary number of Keplerian curves using a Levenburg–Marquardt iteration method. The radial velocity curve is shown in Fig. 5, for which $\gamma = 80.1 \pm 1.8\,{\rm km\,s^{-1}}$, $K = 175.5 \pm 1.0\,{\rm km\,s^{-1}}$, and $T_0 = 1468.2675 \pm 0.0022$ (HJD − 2457000). Errors are derived from the covariance matrix of the orbital solutions. The eccentricity of the orbit was found to be 0.017 ± 0.013. This was not significantly different from zero, so a circular orbit was assumed for the light-curve models.

5 LIGHT CURVE ANALYSIS

The *TESS* light curves of Ton S 415 show low-amplitude variations, with an asymmetric modulation indicative of ellipsoidal deformation of the subdwarf component (Fig. 6). To determine the properties of the binary system, the light curves were modelled using LCURVE software package (described in Copperwheat et al. 2010, appendix A). LCURVE is capable of modelling binary star light curves, accounting for ellipsoidal deformation, gravity darkening, limb darkening, and Doppler beaming. The compact component of the binary was designated as star 1, and the subdwarf component as star 2. The white dwarf is modelled as a sphere, while the subdwarf is modelled as a Roche-distorted spheroid in co-rotation with the binary orbit. Reprocessing of light from the subdwarf by the white dwarf is modelled, but the effect is negligible due to the small size of the white dwarf.

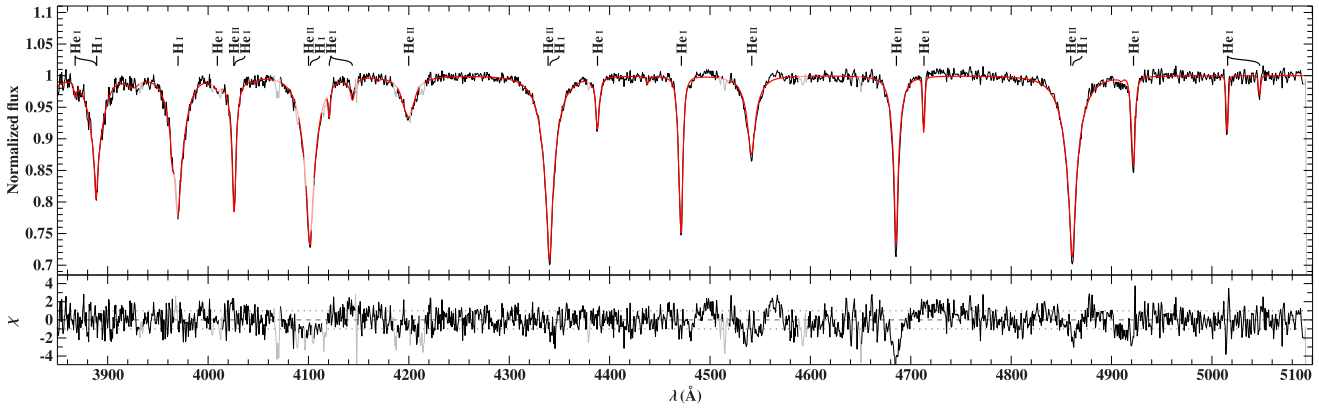

Figure 3. RSS spectrum of Ton S 415 (black) with non-LTE model (red) and residuals (below). Segments in grey were excluded from the fit. The best-fitting solution has $T_{\rm eff} = 43\,380$ K, $\log g/{\rm cm\,s^{-2}} = 5.92$, $\log y = -0.63$ and $v \sin i < 15\,{\rm km\,s^{-1}}$.

Table 2. Parameters of Ton S 415 obtained from SED fit. Uncertainties are given as 1σ of the result.

Property	Value
Colour excess $E(44-55)$	0.0124 ± 0.0020 mag
Extinction parameter $R(55)$ (fixed)	3.02
Angular diameter $\log \Theta$/rad	$-11.038^{+0.006}_{-0.005}$
Parallax ϖ	1.89 ± 0.04 mas
Distance d (*Gaia*)	528 ± 11 pc
Effective temperature $T_{\rm eff}$ (prescribed)	$43\,300 \pm 1000$ K
Surface gravity $\log g/{\rm cm\,s^{-2}}$ (prescribed)	5.89 ± 0.10
Helium abundance $\log y$ (prescribed)	-0.62 ± 0.10
Radius $R = \Theta/(2\varpi)$	$0.1074^{+0.0025}_{-0.0024}\,R_\odot$
Mass $M = gR^2/G$	$0.33^{+0.09}_{-0.07}\,M_\odot$
Luminosity $L = (R/R_\odot)^2 (T_{\rm eff}/T_{\rm eff,\odot})^4$	$37 \pm 4\,L_\odot$

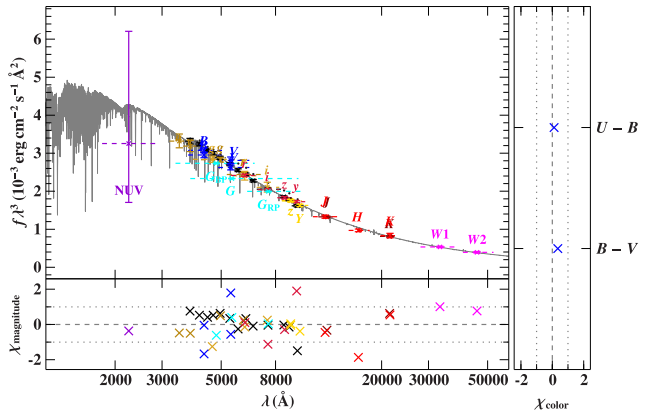

Figure 4. Spectral energy distribution of Ton S 415 with non-LTE model constrained by $T_{\rm eff}$ from the RSS spectrum. Observed magnitudes were obtained in the following systems/surveys: *GALEX* (violet, Bianchi, Shiao & Thilker 2017), *Gaia* (cyan, Gaia Collaboration et al. 2021; Riello et al. 2021), *Gaia* XP box filters (black, De Angeli et al. 2022), Johnson (blue, Girard et al. 2011; O'Donoghue et al. 2013b; Henden et al. 2015), SkyMapper (dark yellow, Onken et al. 2019), SDSS/APASS9 (yellow, Henden et al. 2015), Pan-STARRS (crimson, Magnier et al. 2020), DELVE/DES (bright yellow, Abbott et al. 2021; Drlica-Wagner et al. 2021), VISTA/VHS (dark red, McMahon et al. 2013), 2MASS (red, Skrutskie et al. 2006), WISE (magenta, Schlafly, Meisner & Green 2019).

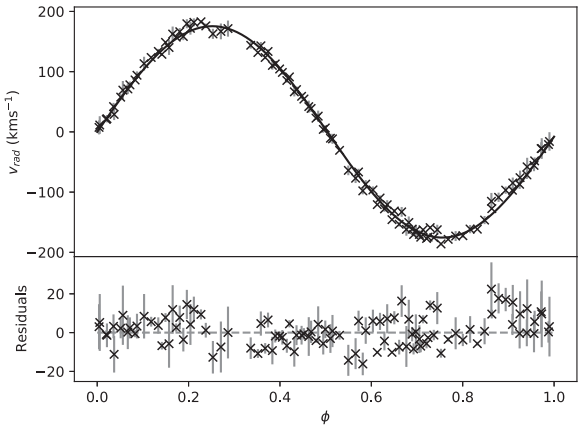

Figure 5. Radial velocity curve of the iHe component of Ton S 415, phased to a period of 0.05884656 d. Data points represent the mean $\Delta v_{\rm rad}$ of the three sections of each spectrum. Error bars derive from the error in $\Delta \ln \lambda$. The radial velocity amplitude is $K = 175.5 \pm 1.0\,{\rm km\,s^{-1}}$.

Limb darkening is modelled in LCURVE using the 4-parameter model of Claret (2000), with each component of the binary requiring four coefficients. Darkening coefficients for the subdwarf component of Ton S 415 were taken from tables computed by Claret (2017) using ATLAS models at $T_{\rm eff} = 44\,000$ K, $\log g/{\rm cm\,s^{-2}} = 5.0$, $\zeta = 0\,{\rm km\,s^{-1}}$. We adopted $a_1 = 1.1276$, $a_2 = -1.9043$, $a_3 = 1.7323$, and $a_4 = -0.5931$ for the limb darkening coefficients, and 0.2487 for the gravity darkening coefficient. Darkening and beaming of the white dwarf component was not modelled due to its contribution to the light curve being negligibly small.

The two available light curves were combined by phasing the data to 0.05884656 d and then binning the flux. 100 bins were used, with the mean flux value being taken in each bin. The error on the binned flux was taken to be the standard deviation of fluxes within the bin, divided by the square root of the number of fluxes.

5.1 Markov chain Monte Carlo modelling

Accurately modelling the light curve of Ton S 415 is complicated by the presence of multiple, strongly correlated, unknown parameters. Most important are the mass ratio $q = M_{\rm sd}/M_{\rm WD}$, the inclination angle i, and the orbital separation a. Adopting a Markov chain Monte

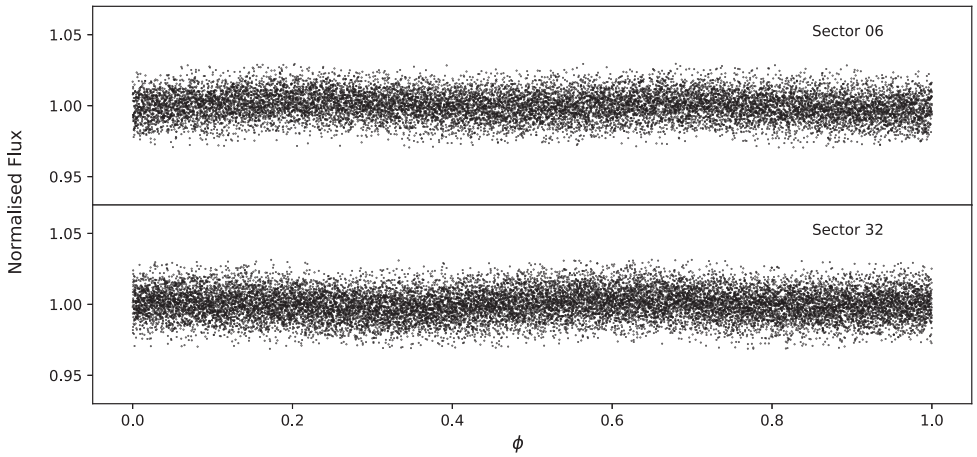

Figure 6. *TESS* light curves of Ton S 415 after de-trending, removal of outliers, and phasing to 0.05884656 d.

Carlo (MCMC) method enables the parameter space to be explored by constructing a large number of individual models, allowing the best-fitting result to be found through χ^2 minimization. A set of initial models is created with parameters either fixed, or randomly initialized within pre-defined ranges. Pairs of models are selected at random and new models are generated by perturbing along the line between them in an N-dimensional space where N is the number of free parameters. The choice of pairs is based on the Bayesian posterior probability of the parameters given the data, $P(a|d)$, as well as the χ^2 of each model. User-defined prior functions may be used to deliberately limit the available jumps to constrain parameters within some desired range. For example, a Gaussian prior of the form

$$P(a|d) = \frac{-((a-b)/\sigma)^2}{2} \tag{2}$$

can be used to restrict the value of parameter a to within 1σ of b.

The temperature and surface gravity of the subdwarf were fixed to $T_{\rm eff} = 43\,330 \pm 1000$ K and $\log g/{\rm cm\,s^{-2}} = 5.89 \pm 0.10$. The radial velocity amplitude of the subdwarf was fixed at $K_{\rm sd} = 175.5 \pm 1.0\,{\rm km\,s^{-1}}$, based on the amplitude of Fig. 5. The orbital period was fixed to 0.05884656 d, taken from the *TESS* periodogram. The Doppler beaming factor $B \equiv (3-\alpha)$ was fixed at 1.23, based on the effective temperature and the *TESS* bandpass, using the formula of Loeb & Gaudi (2003). The mass ratio q and inclination angle i were left free and unconstrained. The scaled stellar radius $r_{\rm sd} = R_{\rm sd}/a$ was kept free, but constrained using priors to keep $R_{\rm sd}$ close to the value of $0.1072 \pm 0.0025\,R_\odot$ derived from the SED. The sum of unprojected orbital speeds was similarly constrained based on $K_{\rm sd}$, q, and i:

$$-2\ln(P(v_{\rm sum}|d)) = \chi^2 + \left(\frac{v_{\rm sum} - \frac{K_{\rm sd}}{\sin i}(1+q^{-1})}{10}\right)^2 \tag{3}$$

Correlation coefficients for all parameter pairs were obtained using LCURVE by fitting light curves to the data using a Levenburg–Marquardt method with a given pair of parameters kept free and all others fixed. The coefficients are shown in Table 3.

In total, 200 groups of models were evaluated for 1000 trials per group. Parameter results were saved every 10 trials for a total output of 20 000 sets. The distribution of q and i is shown in Fig. 7. The majority of models are clustered within a range of $0.4 \leq q \leq 1.0$, $25^\circ \leq i \leq 39^\circ$. The variation of χ^2 for models in this region is low (< 3 per cent), making it difficult to select a best-fitting set of parameters. The adopted mass ratio $q = 0.7 \pm 0.3$ was taken from the median of models within the 67 per cent contour, with

Table 3. Correlation coefficients for the variable parameters used in the MCMC simulations.

	q	i	$r_{\rm sd}$	$v_{\rm sum}$	B
q		0.99	0.98	0.19	−0.14
i			−0.98	−0.22	0.16
$r_{\rm sd}$				−0.01	0
$v_{\rm sum}$					0

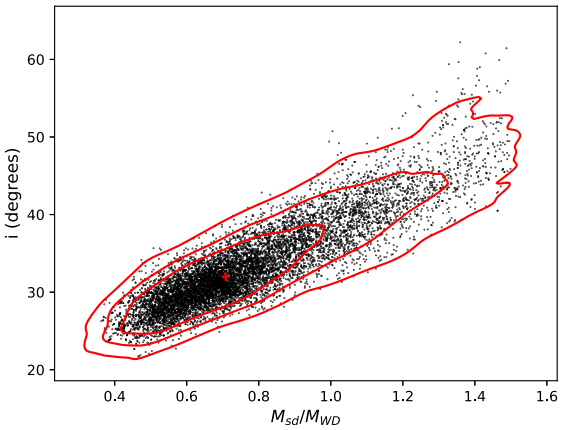

Figure 7. Mass ratios and inclination angles of MCMC models. Half of the computed models are shown. Contours enclose 67, 90, and 99 per cent of all models. The cross indicates the position of the median at $q = 0.7$, $i = 32^\circ$.

the error being half the width of the contour (Fig. 7). With $M_{\rm sd}$, p, and Kepler's third law, this gives $a = 0.59\,R_\odot$ and $i = 35.9^\circ$. The parameters of the Ton S 415 binary system are summarized in Table 4. A comparison of the binned light curve and a model constructed with the adopted parameters is shown in Fig. 8. The asymmetry in the peak heights caused by beaming is reproduced by the model, though the asymmetric flux minima caused by gravity darkening are less well-produced. Gravity darkening coefficients computed for higher-gravity hot subdwarf atmospheres may yield an improved fit, but these were not available for this analysis. The system parameters were found to be insensitive to changes in the assumed gravity darkening coefficient over a range of 0.2−0.3. The resulting variances in q and i were found to be <0.05 and <0.5°, respectively. The effect

Table 4. Parameters of the components and orbit of the Ton S 415 binary system. Values for the iHe binaries OW J0741 (Kupfer et al. 2017) and ZTF J2130+4420 (Kupfer et al. 2020) are shown for comparison.

Property	Ton S 415	OW J0741	ZTF J2130
$T_{\rm eff}$ (K)	$43\,330 \pm 1000$	$39\,400 \pm 500$	$42\,400 \pm 300$
$\log g$ (cm s^{-2})	5.89 ± 0.10	5.74 ± 0.09	5.77 ± 0.05
$\log y$	-0.62 ± 0.10	-0.14 ± 0.06	-0.52 ± 0.03
p (d)	0.058 846 56	0.031 0158	0.027 3195
i (deg)	35.9 ± 7.0	57.4 ± 4.7	86.4 ± 1.0
a (R$_\odot$)	0.59 ± 0.31	0.41 ± 0.04	0.367 ± 0.004
$K_{\rm sd}$ (km s^{-1})	175.5 ± 1.0	422.5 ± 21.5	418.5 ± 2.5
$q = M_{\rm sd}/M_{\rm WD}$	0.7 ± 0.3	0.32 ± 0.10	0.617 ± 0.015
$M_{\rm sd}$ (M$_\odot$)	$0.33^{+0.09}_{-0.08}$	0.23 ± 0.12	0.337 ± 0.015
$M_{\rm WD}$ (M$_\odot$)	$0.47^{+0.24}_{-0.23}$	0.72 ± 0.17	0.545 ± 0.020
$R_{\rm sd}$ (R$_\odot$)	$0.1072^{+0.0025}_{-0.0024}$	0.11 ± 0.02	0.125 ± 0.005

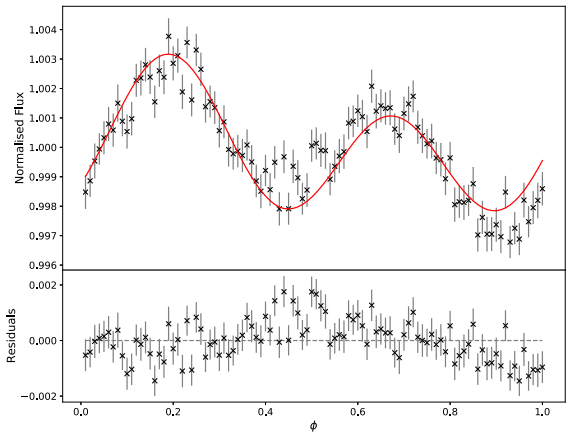

Figure 8. Comparison of binned, phased light curve of Ton S 415 with an LCURVE model created using the parameter results from the MCMC simulations.

on χ^2 was < 1 per cent, with the χ^2 minimum corresponding to a coefficient of 0.245.

6 DISCUSSION

Table 4 compares the derived parameters of Ton S 415 with those of the close iHe sdOB binaries OW J074106.0−0.294811.0 and ZTF J2130+4420. Of the three, Ton S 415 is the hottest, least He-rich, and has the longest orbital period. In terms of atmospheric parameters and component masses, it resembles ZTF J2130 most closely. The main differences are that neither component of Ton S 415 fills its Roche lobe, and there is no evidence of an accretion disc. Additionally, the rotation of Ton S 415 is not synchronized to the orbital period, which would require $v \sin i \simeq 90$ km s^{-1}. This is not unexpected, as the synchronization time-scales of close hot subdwarf binaries are typically long compared to the extended horizontal branch lifetime. The comparison star ZTF J2130 is synchronized, as its smaller orbital separation results in a ∼200 times shorter synchronization time-scale compared to Ton S 415 (Preece, Tout & Jeffery 2018).

Like both comparison stars, Ton S 415 is below the canonical hot subdwarf mass of ~ 0.47 M$_\odot$ and therefore has not evolved via the conventional channel, in which the hydrogen envelope is stripped at the tip of the red giant branch (RGB). Kupfer et al. (2020) modelled ZTF J2130 using a $2.5 - 2.8$ M$_\odot$ progenitor that ignites non-degenerate He burning before reaching the core mass required for a degenerate He flash. Once core He burning begins, most of the envelope mass is removed and the star evolves to become a relatively low-mass, low-luminosity hot subdwarf. The core burning phase lasts for about 500 Myr until He is exhausted and the star evolves to hotter temperatures until residual H in the envelope begins shell burning. The stellar radius grows until the star overfills its Roche lobe and begins accreting onto the white dwarf (WD) companion. Mass transfer proceeds until H burning is exhausted and the subdwarf contracts towards the white dwarf sequence.

Like ZTF J2130 (Kupfer et al. 2020), Ton S 415 is kinematically young, the *Gaia* DR3 proper motions and our system velocity imply membership of the Galactic thin disc.

The atmospheric parameters of Ton S 415 match well with the evolutionary tracks computed by Kupfer et al. (2020) for a core mass of 0.33 M$_\odot$, which is also close to our derived mass. $T_{\rm eff}$ and $\log g$ place both Ton S 415 and ZTF J2130 in the post-H shell ignition phase. Ton S 415 lies further along the track, where mass transfer has either ceased, or never began in the first place due to the greater orbital separation. The most likely outcome for Ton S 415 is that it will evolve into a double white dwarf binary. The orbital period will gradually decrease at a rate $\sim 4 \times 10^{-13}$ s s^{-1} as energy is lost through gravitational radiation. It should be detectable on a time-scale of tens of years, but some five times slower than for ZTF J2130. If the true mass ratio is smaller than ∼0.67, the system may form a stably accreting AM CVn system (Marsh, Nelemans & Steeghs 2004; Solheim 2010). Otherwise, the system will most likely merge to form an R CrB star (Webbink 1984; Saio & Jeffery 2002), on a time-scale ∼ 100 Myr (Peters & Mathews 1963).

7 CONCLUSIONS

Ton S 415 is identified as an intermediate helium hot subdwarf in a highly compact binary system with an unseen white dwarf companion. From *TESS* photometry and SALT RSS spectroscopy, the orbital period is found to be $p = 0.05884656$ d (84.739 min) with a radial velocity amplitude $K_{\rm sd} = 175.5 \pm 1.0$ km s^{-1}. A non-LTE model atmosphere analysis of the RSS spectrum of the hot subdwarf gives the effective temperature $T_{\rm eff} = 43\,300 \pm 1000$ K, surface gravity $\log g = 5.89 \pm 0.10$, and surface helium abundance $\log y = -0.62 \pm 0.10$. The spectral energy distribution gives a radius $R_{\rm sd} = 0.1074 \pm 0.0025$ $R_\odot$. The gravity and radius imply a mass for the hot subdwarf $M_{\rm sd} = 0.33 \pm 0.09$ M$_\odot$. By fitting a large number of light curve models to the data using an MCMC approach with LCURVE, we estimate the system to have a mass ratio of $q = 0.7 \pm 0.3$ and an inclination angle of $i = 32 \pm 7^\circ$. Given the companion mass of $0.47^{+0.24}_{-0.23}$M$_\odot$, the absence of light from the companion in the spectrum or spectral energy distribution, and the lack of space with the orbit for a larger star, we argue that the companion must be a white dwarf. Ton S 415 thus resembles the known intermediate helium subdwarf binary ZTF J2130+4420, and its parameters are consistent with evolution tracks computed by Kupfer et al. (2020). The system is therefore likely to be a post-common-envelope binary that formed from a progenitor that lost its hydrogen envelope before reaching the tip of the RGB, hence the lower mass compared to the ~ 0.47 M$_\odot$ canonical mass for hot subdwarfs. The system will eventually evolve to a double-WD binary and the orbital period will shrink due to gravitational wave radiation. Eventually the system will

either form a stably accreting AM CVn system, or merge to form an R CrB star.

ACKNOWLEDGEMENTS

The authors wish to thank Dr Naomi Titus for providing the data reduction pipeline, Dr Ingrid Pelisoli for providing the Markov chain Monte Carlo wrapper for LCURVE, and Mr Asish Philip Monai for assessing the kinematics of Ton S 415.

Some of the observations reported in this paper were obtained with the SALT under program 2021-1-MLT-005 (PI Jeffery). This paper includes data collected by the *TESS* mission. Funding for the *TESS* mission was provided by the NASA'S Science Mission Directorate. EJS was supported by the United Kingdom Science and Technology Facilities Council (STFC) via UK Research and Innovations (UKRI) doctoral training grant ST/R504609/1. CSJ was supported by the STFC via UKRI research grant ST/V000438/1. The Armagh Observatory and Planetarium (AOP) was funded by direct grant from the Northern Ireland Department for Communities. This also provided funding for AOP membership of the United Kingdom SALT consortium (UKSC). SS acknowledges financial support from AOP in the form of an internship organized by the International Association for the Exchange of Students for Technical Expertize (IAESTE). For the purpose of open access, the authors have applied a Creative Commons Attribution (CC BY) license to any Author Accepted Manuscript version arising.

This research made use of LIGHTKURVE, a PYTHON package for *Kepler* and *TESS* data analysis (Lightkurve Collaboration 2018).

DATA AVAILABILITY

A copy of the SALT data may be made on reasonable application to the authors. The SALT data will be available from the SALT Data Archive (https://ssda.saao.ac.za) after the proprietary period ends in 2025 April. *TESS* photometric data are available through the MAST portal (https://mast.stsci.edu).

REFERENCES

Abbott T. M. C. et al., 2021, ApJS, 255, 20
Bianchi L., Shiao B., Thilker D., 2017, ApJS, 230, 24
Chavira E., 1958, Bol. Obs. Tonantzintla Tacubaya, 3, 15
Claret A., 2017, A&A, 600, A30
Claret A., 2000, A&A, 363, 1081
Copperwheat C. M., Marsh T. R., Dhillon V. S., Littlefair S. P., Hickman R., Gänsicke B. T., Southworth J., 2010, MNRAS, 402, 1824
De Angeli F. et al., 2022, A&A, 674, A2
van Dokkum P. G., 2001, PASP, 113, 1420
Dorsch M., Jeffery C. S., Irrgang A., Woolf V., Heber U., 2021, A&A, 653, A120
Drilling J. S., Jeffery C. S., Heber U., Moehler S., Napiwotzki R., 2013, A&A, 551, A31
Drlica-Wagner A. et al., 2021, ApJS, 256, 2
El-Badry K., Rix H.-W., Heintz T. M., 2021, MNRAS, 506, 2269
Fitzpatrick E. L., Massa D., Gordon K. D., Bohlin R., Clayton G. C., 2019, ApJ, 886, 108
Gaia Collaboration et al., 2021, A&A, 649, A1
Girard T. M. et al., 2011, AJ, 142, 15
Green R. F., Schmidt M., Liebert J., 1986, ApJS, 61, 305
Han Z., Podsiadlowski P., Maxted P. F. L., Marsh T. R., Ivanova N., 2002, MNRAS, 336, 449
Han Z., Podsiadlowski P., Maxted P. F. L., Marsh T. R., 2003, MNRAS, 341, 669
Heber U., Hunger K., Jonas G., Kudritzki R. P., 1984, A&A, 130, 119
Heber U., Irrgang A., Schaffenroth J., 2018, Open Astron., 27, 35
Henden A. A., Levine S., Terrell D., Welch D. L., 2015, in American Astronomical Society Meeting Abstracts #225. p. 336.16
Jeffery C. S., Miszalski B., Snowdon E. J., 2021, MNRAS, 501, 623
Kupfer T. et al., 2017, ApJ, 851, 28
Kupfer T. et al., 2020, ApJ, 891, 45
Lightkurve Collaboration, 2018, Astrophysics Source Code Library, record-ascl:1812.013
Lindegren L. et al., 2021, A&A, 649, A4
Loeb A., Gaudi B. S., 2003, ApJ, 588, L117
Magnier E. A. et al., 2020, ApJS, 251, 6
Marsh T. R., Nelemans G., Steeghs D., 2004, MNRAS, 350, 113
Maxted P. F. L., Heber U., Marsh T. R., North R. C., 2001, MNRAS, 326, 1391
McMahon R. G., Banerji M., Gonzalez E., Koposov S. E., Bejar V. J., Lodieu N., Rebolo R., VHS Collaboration, 2013, The Messenger, 154, 35
Morris S. L., 1985, ApJ, 295, 143
Naslim N., Jeffery C. S., Ahmad A., Behara N. T., Şahìn T., 2010, MNRAS, 409, 582
Naslim N., Geier S., Jeffery C. S., Behara N. T., Woolf V. M., Classen L., 2012, MNRAS, 423, 3031
O'Donoghue D., Kilkenny D., Koen C., Hambly N., MacGillivray H., Stobie R. S., 2013a, MNRAS, 431, 240
O'Donoghue D., Kilkenny D., Koen C., Hambly N., MacGillivray H., Stobie R. S., 2013b, MNRAS, 431, 240
Onken C. A. et al., 2019, PASA, 36, e033
Peters P. C., Mathews J., 1963, Phys. Rev., 131, 435
Preece H. P., Tout C. A., Jeffery C. S., 2018, MNRAS, 481, 715
Riello M. et al., 2021, A&A, 649, A3
Saio H., Jeffery C. S., 2002, MNRAS, 333, 121
Savitzky A., Golay M. J. E., 1964, Anal. Chem., 36, 1627
Schlafly E. F., Meisner A. M., Green G. M., 2019, ApJS, 240, 30
Skrutskie M. F. et al., 2006, AJ, 131, 1163
Solheim J.-E., 2010, PASP, 122, 1133
Stobie R. S., Kilkenny D., O'Donoghue D., 1995, Ap&SS, 230, 101
Webbink R. F., 1984, ApJ, 277, 355
Wegner G., 1979, AJ, 84, 1384
Wegner G., 1980, AJ, 85, 538
Wright J. T., Howard A. W., 2009, ApJS, 182, 205
Wu Y., Chen X., Li Z., Han Z., 2018, A&A, 618, A14
Zhang X., Jeffery C. S., 2011, MNRAS, 419, 452

This paper has been typeset from a TEX/LATEX file prepared by the author.